

Physical and psychophysical characterization of a novel clinical system for digital mammography

Stefano Rivetti

*Department of Physics, Alma Mater Studiorum, University of Bologna, Bologna 40127, Italy
and Struttura Complessa di Fisica, Sanitaria "Azienda USL di Modena," Modena 41100, Italy*

Nico Lanconelli^{a)}

Department of Physics, Alma Mater Studiorum, University of Bologna, Bologna 40127, Italy

Marco Bertolini and Giovanni Borasi

Arcispedale Santa Maria Nuova, Reggio Emilia 42123, Italy

Paola Golinelli and Domenico Acchiappati

Struttura Complessa di Fisica, Sanitaria "Azienda USL di Modena," Modena 41100, Italy

Ennio Gallo

Department of Radiology, Azienda Ospedaliera Universitaria Policlinico di Modena, Modena 41100, Italy

(Received 25 March 2009; revised 27 August 2009; accepted for publication 21 September 2009; published 9 October 2009)

Purpose: In recent years, many approaches have been investigated on the development of full-field digital mammography detectors and implemented in practical clinical systems. Some of the most promising techniques are based on flat panel detectors, which, depending on the mechanism involved in the x-ray detection, can be grouped into direct and indirect flat panels. Direct detectors display a better spatial resolution due to the direct conversion of x rays into electron-hole pairs, which do not need an intermediate production of visible light. In these detectors the readout is usually achieved through arrays of thin film transistors (TFTs). However, TFT readout tends to display noise characteristics worse than those from indirect detectors. To address this problem, a novel clinical system for digital mammography has been recently marketed based on direct-conversion detector and optical readout. This unit, named AMULET and manufactured by FUJIFILM, is based on a dual layer of amorphous selenium that acts both as a converter of x rays (first layer) and as an optical switch for the readout of signals (second layer) powered by a line light source. The optical readout is expected to improve the noise characteristics of the detector. The aim is to obtain images with high resolution and low noise, thanks to the combination of optical switching technology and direct conversion with amorphous selenium. In this article, the authors present a characterization of an AMULET system.

Methods: The characterization was achieved in terms of physical figures as modulation transfer function (MTF), noise power spectra (NPS), detective quantum efficiency (DQE), and contrast-detail analysis. The clinical unit was tested by exposing it to two different beams: 28 kV Mo/Mo (namely, RQA-M2) and 28 kV W/Rh (namely, W/Rh).

Results: MTF values of the system are slightly worse than those recorded from other direct-conversion flat panels but still within the range of those from indirect flat panels: The MTF values of the AMULET system are about 45% and 15% at 5 and 8 lp/mm, respectively. On the other hand, however, AMULET NNPS results are consistently better than those from direct-conversion flat panels (up to two to three times lower) and flat panels based on scintillation phosphors. DQE results lie around 70% when RQA-M2 beams are used and approaches 80% in the case of W/Rh beams. Contrast-detail analysis, when performed by human observers on the AMULET system, results in values better than those published for other full-field digital mammography systems.

Conclusions: The novel clinical unit based on direct-conversion detector and optical reading presents great results in terms of both physical and psychophysical characterizations. The good spatial resolution, combined with excellent noise properties, allows the achievement of very good DQE, better than those published for clinical FFDM systems. The psychophysical analysis confirms the excellent behavior of the AMULET unit. © 2009 American Association of Physicists in Medicine.

[DOI: [10.1118/1.3245879](https://doi.org/10.1118/1.3245879)]

Key words: digital mammography, direct-conversion detector, amorphous selenium, optical readout

I. INTRODUCTION

In the past decade, many approaches for developing full-field digital mammography (FFDM) systems have been investigated and tested. The most promising techniques implemented in commercial units are based on solid-state flat panel (FP) detectors. FPs can be grouped into two main classes: Direct and indirect detectors, depending on the mechanism used in the x-ray detection. In the first case, x-ray photons are directly converted into electron-hole pairs within a photoconductive layer usually made of amorphous selenium (*a*-Se). In the second case, x rays are first converted into visible light in a scintillation crystal and, subsequently, the light is converted into electric charge in a photosensitive element. The imaging characteristics of the direct and indirect FPs can differ noticeably given that the image formation process in the two detectors is considerably different. On one hand, direct-conversion systems based on *a*-Se present an excellent spatial resolution and appear to be the most promising for any application below 100 keV, according to Hajdok *et al.*¹ On the other hand, *a*-Se detectors show worse noise characteristics when compared to other systems.²⁻⁴ Many approaches have been explored for reading out signals in *a*-Se plates.⁵⁻⁷ Currently, to our knowledge, all the commercial FFDM systems consisting of *a*-Se detectors employ a readout based on an active matrix array of thin film transistors (TFTs).⁸

In order to improve on the noise limits associated with the standard readout of *a*-Se detectors, a novel clinical FFDM system (named AMULET) has been manufactured by FUJIFILM and recently introduced in the market. The AMULET detector comprises a direct-conversion, light-reading radiation solid-state detector based on an *a*-Se plate. The detector consists of a dual layer of *a*-Se: The x rays are converted into electrical signals in the first layer and are read out in the second layer by means of an optical switch. As an alternative to the TFT readout commonly used for FPs, in this system light is used as a switch for reading out electrical signals. In fact, the detector collects the image information by storing the radiation that has passed through the breast as an electrostatic latent image. Afterward, an electric current depending on the latent image is generated when the detector is scanned by a reading light applied from a dedicated source. This source consists of a linear array of LEDs and an optical system for applying a line of reading lights to the detector. The line source moves along one direction in such a way that the entire surface of the detector can be scanned. The combination of direct conversion and the optical switching technology is supposed to provide high resolution images with low noise.

The assessment of the image quality of a digital detector from a physical point of view is usually performed by measuring objective figures such as modulation transfer function (MTF), noise power spectra (NPS), and detective quantum efficiency (DQE). These metrics measure features linked to spatial resolution, contrast, and noise and are very useful for characterizing a clinical system. However, these figures alone are often not enough to grasp hints about the image

quality from a clinical perspective. To this end, a characterization, which involves human observers, can be more effective. *Ad hoc* phantom images can be acquired and read out by humans for assessing the contrast-detail (CD) visibility of predetermined objects of various sizes and contrasts. The combination of physical measurements and CD analysis allows one to achieve a more accurate evaluation of the investigated imaging system.

The aim of this paper is to realize a characterization of a novel clinical FFDM unit based on a direct-conversion detector and optical readout (FUJIFILM AMULET) in terms of physical figures of merit (MTF, NPS, and DQE) and psychophysical parameters (CD analysis).

II. MATERIALS AND METHODS

A wide range of uniform exposures was used to calculate the system response curve. From a region of interest (ROI) close to the chest wall section of the detector, the average pixel intensity was computed. We then performed a characterization of the FUJIFILM AMULET unit by measuring both physical properties, such as MTF, NPS, DQE, and psychophysical figures (CD analysis). All acquisitions were obtained on a clinical unit without compression paddle and antiscatter grid. We acquired images by using two different spectra: 28 kVp Mo/Mo (molybdenum anode with 30 μ m molybdenum filter, namely, RQA-M2, according to IEC-61267 standard) and 28 kVp W/Rh (tungsten anode with 50 μ m rhodium filter).⁹ We attached a 2 mm thick foil of aluminum to the x-ray tube for simulating a low scatter condition. The exposure to the detector was measured for each investigated condition with a calibrated mammographic ionization chamber (UNFORS Xi, Unfors Instruments, Billdal, Sweden). The source-to-image distance is nearly 65 cm.

AMULET employs the same image processing technology used by FUJIFILM for their FCR mammography systems. In fact, the readout system generates 16 bit linear data, and a subsequent logarithmic transform is applied to the data, giving rise to a 12 bit image. The 16 bit linear image is not accessible to users, whereas the 12 bit data are made available through one of the processing modes. Users are required to choose among one of the processing methods (automatic, semiautomatic, FIX-mode, and others). The FIX-mode is the only one that allows users to select the sensitivity (*S*) and latitude (*L*) values, such that the pixel values in the resultant image are directly linked to exposure in a manner that mimics a film screen system. All the images used in this work were acquired with the FIX-mode processing with parameters *S* and *L* equal to 121 and 2, respectively. The system was calibrated using standard clinical procedures.

II.A. Description of the investigated system

The main characteristics of the investigated FFDM system are summarized in Table I. The relevant advancement is in the combination of a direct-conversion detector based on *a*-Se and an optical readout system, instead of the typical TFT readout used for FFDM detectors. Figure 1 shows a sketch of the dual layer detector employed in the AMULET

TABLE I. Main characteristics of the investigated FFDM system.

Manufacturer	FUJIFILM
System	AMULET
Detection type	Direct conversion
Readout	Optical reading
Detector material	<i>a</i> -Se
Imaging area (cm × cm)	18 × 24
Array size	3540 × 4740
Pixel pitch (μm)	50
Image depth (bits)	12

system. The detector consists of six main components: A negative top electrode, a thick x-ray photoconducting layer (PCL), an electron trapping layer (ETL), a thin readout PCL, stripe electrodes, and an optical source. The x-ray PCL is made of a layer of *a*-Se with a thickness of less than 200 μm.¹⁰ In this setup, x-ray photons are directly converted into electron-hole pairs. Then, by using a strong electric field, the generated electrons are accumulated on the ETL, where a latent electron image is formed. After x-ray exposure, the negative voltage is turned off and the top electrode becomes grounded. Trapped electrons induce positive charges on the stripe electrodes and an electric field in the readout PCL. In the subsequent readout phase, light is irradiated from a linear optical source, which generates electron-hole pairs in the readout PCL. These electrons are drifted and collected on the stripe electrodes, where they are detected as signal charges. The line source moves along a direction perpendicular to the direction of the stripe electrodes (scan direction), while for each position of the line source, data are readout on the direction indicated in Fig. 1 (data line direction). A more complete description of the structure of the detector and its functioning can be found in a paper cited in the reference section.¹⁰

II.B. Physical characterization

Presampling MTF was measured by using the edge technique: An oversampled edge spread function was obtained by a tungsten edge test device (TX5, IBA Dosimetry, Schwarzenbruck, Germany). The NPS was computed according to the International Standard IEC 62220-1-2 at different

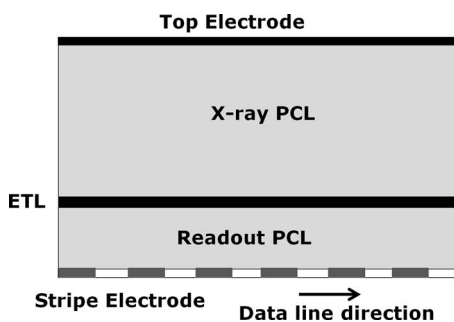


FIG. 1. Sketch of the detector of the AMULET system. The main components of the detector are a negative top electrode, a thick x-ray PCL, an ETL, a thin readout PCL, stripe electrodes, and an optical source.

exposure levels. The mammographic unit was characterized on a wide range of air kerma (20–150 μGy). This range was chosen to be considerably below and above the typical mammographic detector exposure range which according to other studies have a median of about 120 μGy.^{4,11} For each exposure, the 2D NPS was obtained from averaging the Fourier transforms of fixed-size ROIs extracted from four different images. The 1D NPS was then extracted from the 2D NPS on a radial direction (at 45°) and subsequently normalized for the squared mean signal value of the ROI, thus giving the normalized NPS (NNPS). The same ROIs used for calculating the NNPS were also considered to achieve the RSD analysis.² RSD (i.e., standard deviation divided by average signal value) was calculated inside the ROIs. We then fit the average RSD squared over all the ROIs using the following function:

$$\text{RSD}^2 = \left(\frac{\sigma_{\text{tot}}}{x} \right)^2 = \frac{\alpha}{x} + \beta + \frac{\gamma}{x^2}, \quad (1)$$

where x is the x-ray exposure, and α , β , and γ represent the contributions of the quantum-statistical (Poisson) noise source, of a dose related (multiplicative) noise source, and of a dose independent (additive) noise source, respectively. The x-ray photon fluence was gathered from tabulated data and used to calculate the number of photons per unit area at the measured exposure. The DQE is then calculated as

$$\text{DQE}(f) = \frac{\text{MTF}^2(f)}{\text{NNPS}(f, q) \cdot q}, \quad (2)$$

where q is the number of photons per unit area.

II.C. Contrast-detail analysis

Contrast-detail analysis was carried out using the CDMAM 3.4 phantom (Artinis, Medical Systems B.V., Zetten, The Netherlands). It consists of a matrix of squares, each one containing two identical gold disks of given thickness and diameter. One disk is placed at the center and the second in a randomly chosen corner. The observer has to indicate the corner where the eccentric disk is located. The phantom covers a range of object sizes and thicknesses representing microcalcifications and small masses. The object thicknesses range between 0.03 and 2 μm of gold, resulting in a radiation contrast range of about 0.5%–30% at standard mammography exposure conditions. Images were acquired in the same conditions used for the DQE calculation. No additional Plexiglas plates were placed below or above the phantom. The smallest details of the CDMAM were placed close to the chest wall side. The CD analysis was carried out in two different ways: With human observers and with a software that performs an automatic reading (CDCOM).¹² Human observers evaluated images on two dedicated high resolution reference monitors (Barco MGD521, 2048 × 2560 matrix, 8 bits, max luminance: 600 cd/m²). The images were displayed on the monitors with the room light off and the same ambient illumination for all the readers. The visualization parameters (brightness, contrast, and magnification factor) were fixed to the same value for all the observers. Readers

operated at the same distance from the monitors and had all the time they needed for reading each phantom image. Five experienced operators evaluated the phantom images by using specific software developed by our group and already tested for the evaluation of FFDM systems and freely available at www.df.unibo.it/medphys.² Six images were acquired for each exposure and shown randomly to the observers. In order to obtain different realizations of the nonstochastic noise, the position of the CDMAM phantom was changed after each acquisition. For the two investigated spectra, the read images were acquired at an exposure of 70 μGy (air kerma at the detector entrance). For each reading of the phantom a CD curve was estimated, by fitting the reading data with a Weibull function. Furthermore, three different quantities were computed for describing the performance of the readers: Correct observation ratio (COR), image quality figure (IQF), and IQF_{inv} defined as follows:

$$\text{COR} = \frac{\text{Correct observations}}{\text{Total number of squares}} \cdot 100\%, \quad (3)$$

$$\text{IQF} = \sum_{i=1}^{16} C_i \cdot D_{i,\min}, \quad (4)$$

$$\text{IQF}_{\text{inv}} = \frac{100}{\text{IQF}}. \quad (5)$$

Here $D_{i,\min}$ represents the threshold diameter in contrast column i .

The reading of CDMAM phantoms by human observers presents two main drawbacks. First, remarkable interobserver errors can arise. Second, the human reading is very time consuming. In order to overcome these weaknesses, automatic methods can be used to get contrast-detail results from phantom images. In fact, nowadays software is available for the automatic reading of the CDMAM images. For instance, CDCOM is a well known and freely available software developed by the Radiology Department of the University Medical Centre in Nijmegen (The Netherlands).¹² CDCOM achieves the automatic reading of the CDMAM phantoms by performing various steps. The first process consists of the detection of the borders of the phantom by using the Hough transform and subsequent estimation of the center of each cell. The average pixel value of four ROIs located near the corners is then calculated for each cell. The position of the eccentric disk is supposed to be within the ROI with the highest average value. The detection fraction of each cell is then calculated by using a set of images acquired at the same exposure. In this work the results were fitted with the same psychometric curve used with human observers (Weibull function). In addition, we also reported CD curves obtained with the CDMAM analyzer software (Artinis, Medical Systems B.V., Zetten, The Netherlands). This program gives the user reports of the quality of the images obtained starting from the same CDCOM readings. The results obtained from the six images acquired for each exposure were then averaged. A comparison between the CD curves obtained and the theoretical data estimated from the Rose model was also

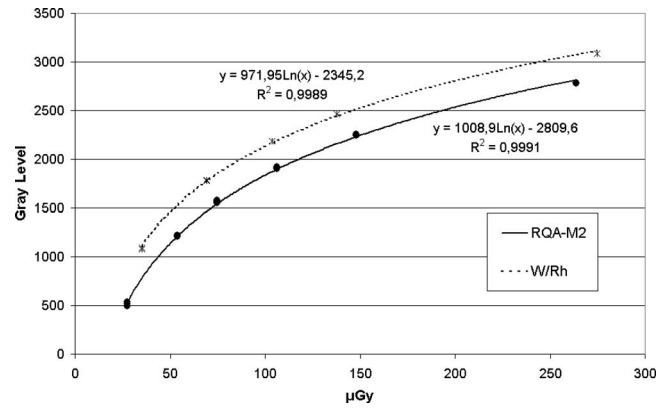


FIG. 2. Response curves for the two investigated beams (RQA-M2 and W/Rh). In both cases, the response is logarithmic and the functions used for fitting are shown within the plot.

evaluated.¹³ According to this model, for a circular target of diameter α , the contrast threshold (C_{TR}) can be assessed as follows:

$$C_{\text{TR}} = \frac{2k}{\alpha \sqrt{\pi \cdot q \cdot \text{DQE}(0)}}, \quad (6)$$

where $\text{DQE}(0)$ is the DQE at zero spatial frequency and k represents the minimum SNR threshold needed by the observer for detecting the object. Statistical analysis of the CD curves was carried out using the SPSS package (version 13.0; SPSS Inc., Chicago, IL). In fact, we tested when two CD curves are statistically significantly different by performing a nonparametric test (Mann–Whitney). A p value of less than 0.05 was considered to indicate a statistically significant difference between two curves.

III. RESULTS

III.A. Physical characterization

Figure 2 shows the response of the system under different conditions. The experimental data were fitted with the logarithmic function shown in the plots. Note that the system has a logarithmic behavior for both the investigated beams, like most of the computed radiography systems.^{14–16} The physical characterization was then performed on linearized images, according to IEC Standards (IEC-62220-1-2).¹⁷

Figure 3(a) shows the MTF curves measured for the RQA-M2 beam on the two orthogonal directions (scan and data line, as described in Sec. II A). To calculate the DQE, the mean of the MTF along the two orthogonal directions was estimated. Figure 3(b) shows the MTF averaged over the two directions for the two investigated beams. There is also shown a plot of two MTFs collected from published values for two different FPs: A direct conversion one based on $a\text{-Se}$ plate and an indirect conversion based on CsI scintillator.²

The noise components estimated by the RSD analysis are comparable to those obtained with other FPs.² In particular, the values achieved by fitting Eq. (1) are the following: 0.009, 0.000 017, and 0.8 for the Poisson, multiplicative, and additive contribution, respectively. However, this variance

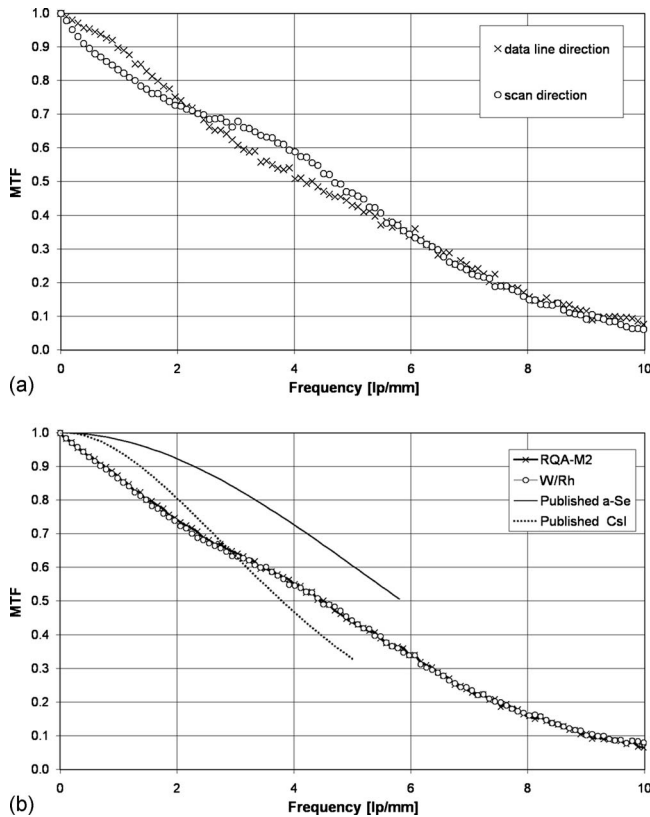


FIG. 3. MTF estimated with the edge technique for the RQA-M2 beam (a) in the two directions (scan and data line). Some conspicuous variations arise between the two directions, especially for frequencies up to 6 lp/mm. In (b) the MTF resulting from the average on the two directions is shown for the two investigated beams. No noticeable differences are observed between the two MTFs. The plot also shows two MTF collected from published values for two FPs: A direct conversion one based on *a*-Se plate and an indirect conversion one based on CsI scintillator.

examination does not provide information about the frequency components of the noise. Figure 4(a) shows an example of a 2D NNPS for the RQA-M2 beam. The gray-level scale bar connects the NNPS values in mm^2 to the gray level of the image. Figure 4(b) shows the 1D NNPS estimated along the two orthogonal axes for the RQA-M2 beam at an exposure of about $150 \mu\text{Gy}$.

Figures 5(a) and 5(b) show the 1D NNPS for the two beams at different exposure levels. These 1D values were calculated from the 2D spectra along a radial line at a direction of 45° and are considered for the subsequent DQE calculation.

In order to assess the uniformity of the noise response, the NNPS was calculated by means of five different ROIs located at various positions within the plate. The *center* ROI is the same one used in calculating the NNPS shown in Fig. 5. Other four ROIs located in the proximity of the four corners of the image, named top left, top right, bottom left, and bottom right were selected, as shown in Fig. 6(a). We measured the exposure for each ROI separately. In fact, a maximum variation of about 20% among the exposures of the five ROIs has been observed. The difference in the radiation field is explained by the heel effect, the increased photon path length

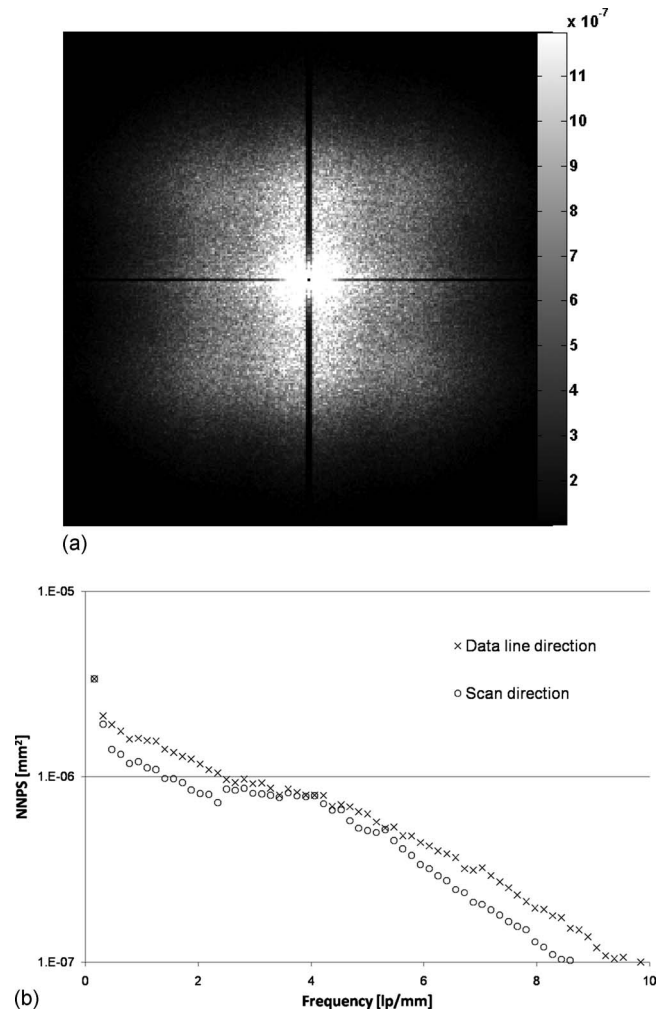


FIG. 4. (a) 2D NPS for the RQA-M2 beam for an exposure of about $150 \mu\text{Gy}$. It is worth noting that the axes' contributions are lowered at almost all the frequencies, and some sort of nonisotropic low-pass filtering seems to have been applied. The same trend can be observed at different exposures and for the other investigated beam. The gray-level bar on the right connects NNPS values in mm^2 to the gray level of the image. (b) 1D NNPS for the RQA-M2 beam for the same exposure estimated on the two orthogonal directions (scan and data line).

through the window of the tube, as well as the inverse square reduction. Figure 6(b) illustrates the product of NNPS and air kerma, measured for each ROI separately. In this way, we considered only variation due to the detection system. In fact, the fluctuations among the different ROIs are confined to a maximum of 3%.

For a strictly quantum noise limited system, the product of the NNPS and the exposure (air kerma) should remain constant for all exposures. It is thus possible to estimate the quantum noise limited condition by observing the value of this product. Figures 7(a) and 7(b) show a plot of this product for the two investigated beams. In Fig. 8 we compare the product of NNPS and exposure for the two investigated beams at an exposure of about $150 \mu\text{Gy}$. The W/Rh beam shows a slightly better noise performance than the RQA-M2 one. Figure 8 also shows some published data of two FPs for digital mammography.² The new data come from two differ-

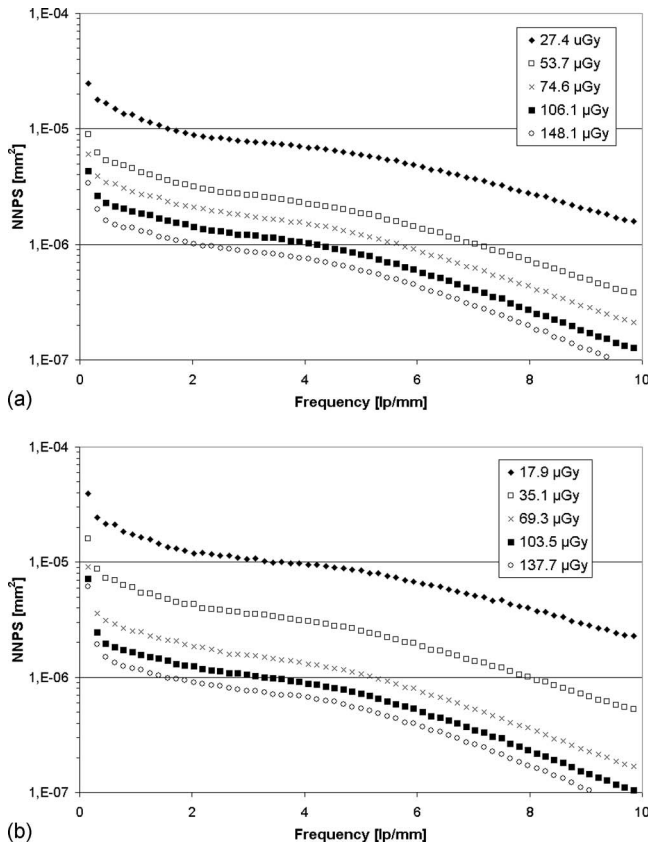


Fig. 5. NNPS for the RQA-M2 (a) and the W/Rh (b) beam at five different exposures. 1D NNPS was computed along a radial line of the 2D NNPS. When considering the same exposure, the W/Rh beam shows a slightly better performance than the RQA-M2 one.

ent FPs: The first based on an *a*-Se detector and the other one based on an indirect CsI scintillator. These data were estimated in the same experimental conditions (same x-ray beam and similar exposure values).

In Figs. 9(a) and 9(b) the DQE results for the two beams at various exposure values are plotted. This system shows a maximum DQE of about 70% for RQA-M2 and nearly 80%

for W/Rh. Figure 10 shows the DQE estimated separately on the two orthogonal axes for the RQA-M2 beam at an exposure of about 150 μ Gy.

III.B. Contrast-detail analysis

Figure 11 depicts the CD curves obtained by human observers for the RQA-M2 and the W/Rh beams at an exposure of about 70 μ Gy. Figure 11 also shows a CD curve obtained from published values as one of the best outcomes from other FFDM systems.² This curve was obtained in the same experimental conditions (x-ray beam RQA-M2, same exposure) and analyzed by human observers with the same software and visualization parameters (magnification, window/level).

Figure 12 illustrates a comparison of CD curves obtained by human observers, automatic methods, and the Rose theoretical model for the RQA-M2 beam at an exposure of about 70 μ Gy. As expected, the automatic reading leads to lower contrasts than those detected by human observers. In fact, the CDMAM analyzer software and the CDCOM results fitted with the Weibull function gave a nearly identical response.

Finally, Table II reports the results of the CDMAM evaluation in terms of the quantities COR, IQF, and IQF_{inv} for the two investigated beams; from both human readings and from those achieved with CDCOM. It is worth noting that when comparing the two beams, no clear difference emerges. However, the W/Rh beam seems to provide a slightly better visibility than the RQA-M2 spectrum, for both human observers and CDCOM data, especially in terms of COR. The reported values from human readers and for CDCOM analysis are better than those from other FFDM systems in similar conditions.^{2,18,19}

IV. DISCUSSION

The MTF of the AMULET system presents non-negligible differences between the two directions (with a maximum of about 10%), especially for frequencies up to 6 lp/mm. The MTF averaged on the two directions is almost identical for

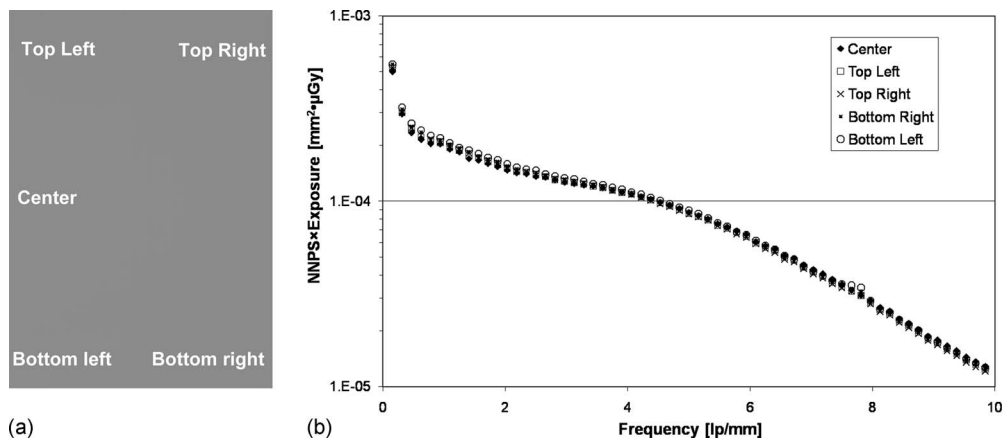


Fig. 6. The NNPS has been computed in five different ROIs within the image as shown in (a): Top left, top right, center (the same ROI used for estimating the NNPS shown in Fig. 5), bottom left, and bottom right. The product of NNPS multiplied by air kerma provides very small differences among the different locations (b). Here, air kerma was measured separately for the different ROIs.

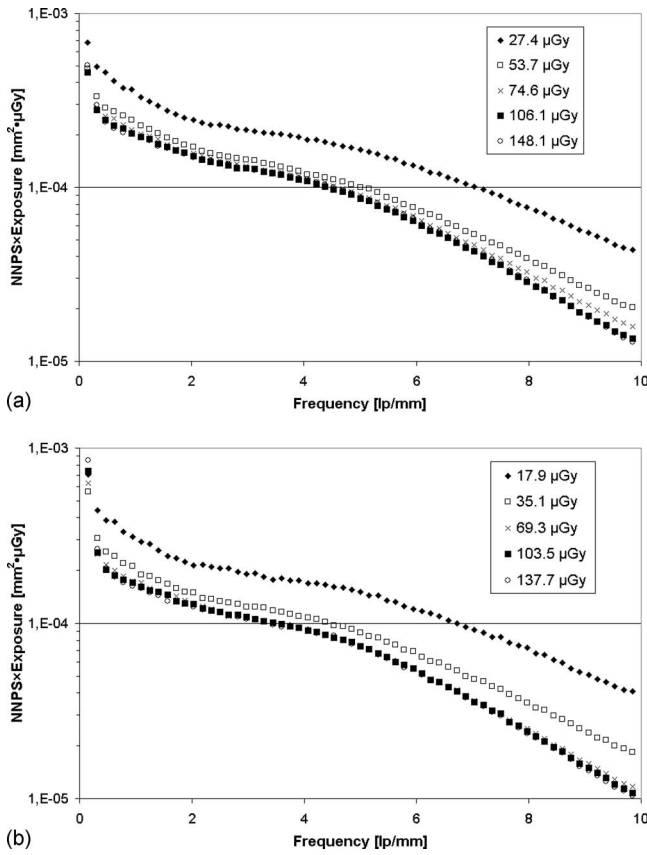


FIG. 7. NNPS multiplied by air kerma for the RQA-M2 (a) and W/Rh (b) beams. This product should be independent of the exposure for a strictly quantum noise limited detector.

the two analyzed beams. Comparing the MTF results to the published values, one can note that the AMULET's MTF despite the smaller pixel size is worse than those from other FFDM systems with *a*-Se plates (with a maximum difference of about 20%), whereas it is fairly comparable to the MTF obtained with FPs based on scintillation phosphors.^{2-4,20}

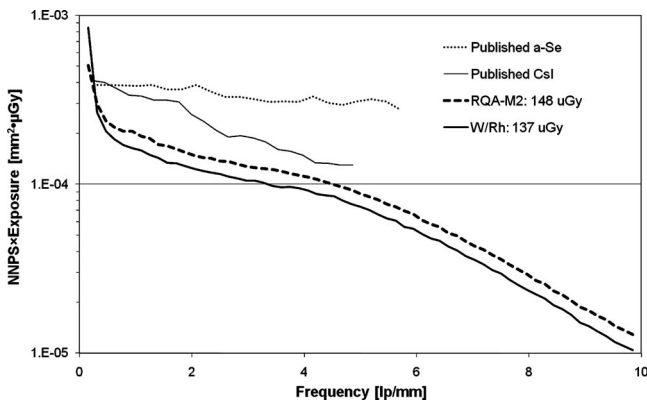


FIG. 8. Comparison of the multiplication between NNPS and air kerma for the two analyzed beams for an exposure of about 140 μGy . The W/Rh beam shows a slightly better performance with respect to the RQA-M2 one. Published data of two FPDs for digital mammography are also reported (a direct-conversion detector based on *a*-Se and an indirect conversion one based on CsI scintillator).

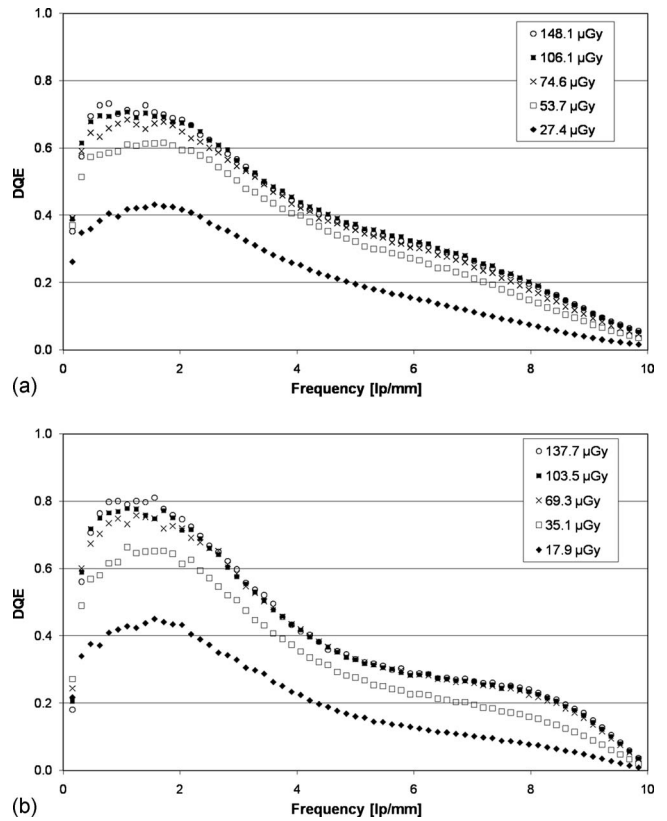


FIG. 9. DQE for the RQA-M2 (a) and the W/Rh (b) beam at five different exposures. The W/Rh beam shows a better performance with respect to the RQA-M2 one even in terms of DQE.

It is worth noting that the 2D noise spectrum presents very low values along the principal axes. These values are visualized in black in Fig. 4(a) and appear along the entire axes, except for points neighboring the origin. The NNPS along the two axes is, on average, about one order of magnitude lower than the noise of the neighbor frequencies. Usually, in FPs based on *a*-Se, a higher noise is found along one or both axes. However, the readout of the AMULET system is completely different from other FPs. The noise contribu-

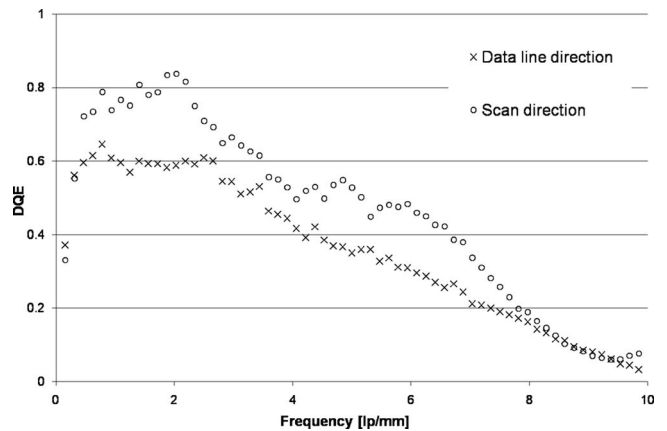


FIG. 10. DQE for the RQA-M2 beam at an exposure of about 150 μGy estimated on the two orthogonal directions. Some differences arise especially at low frequencies.

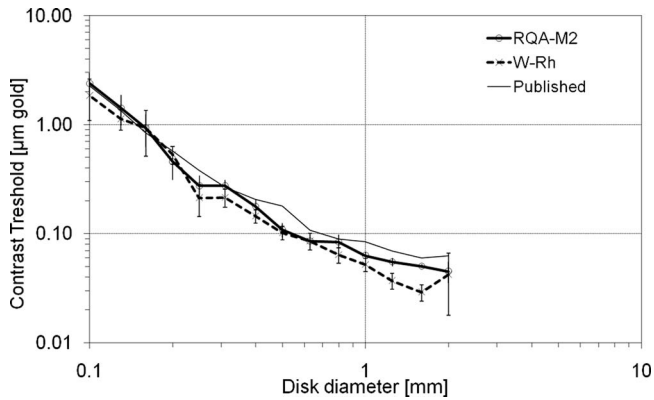


FIG. 11. CD curves obtained by human observers for the two investigated beams at an exposure of about $70 \mu\text{Gy}$. We also plotted a comparison with a CD curve obtained in the same experimental conditions, which represents one of the best published values for FFDM systems. The error bars correspond to ± 1 standard error from the mean.

tion along the axes is lowered through a filtering process by the software. This filtering is integrated in the reading step and users have no control on it. This process is designed to remove banding nonuniformities in the vertical and horizontal directions. Besides, the system appears to have a slight different behavior between the two directions. In fact, the trend of the NNPS is slightly different since the noise in the scan direction has a great drop at low frequencies (up to 2 lp/mm), whereas it remains essentially constant for frequencies in the range of 2–4 lp/mm. For frequencies greater than 4 lp/mm, the noise in the two directions basically decreases with similar trend. This behavior is very similar to the one observed for the MTF calculated on the two directions even if in that case the differences were less pronounced. The difference in the noise in the two directions reaches a maximum of about 30%.

When considering the same exposure, the W/Rh beam shows a slight better performance than the RQA-M2 one in terms of NNPS. Further, the AMULET unit demonstrates a NNPS decreasing with frequency, whereas systems based on direct conversion generally present relatively flat NNPS values. The lower NNPS at high frequencies is related to the lower MTF of the system due to the optical readout method. By comparing these NNPS values to the published data for FFDM systems, it turns out that the AMULET exhibits better noise outcomes since its NNPS is lower for almost the entire range of frequencies.^{2–4} This confirms that the optical readout provides better noise characteristics with respect to the readout employed in FPs. In fact, AMULET does not present an additive noise lower than other FPs, as resulting from the RSD analysis. Nevertheless, NNPS results suggest that most of the noise is confined at very low frequencies. We would like to remark that the lower noise cannot be attributed to an increased thickness of the *a*-Se layer since the AMULET detector has a PCL with a thickness of less than $200 \mu\text{m}$, while other systems based on *a*-Se have thicknesses equal to or greater than $200 \mu\text{m}$.²⁰

Note that the product of the NNPS multiplied by the exposure is almost constant for most of the exposures except

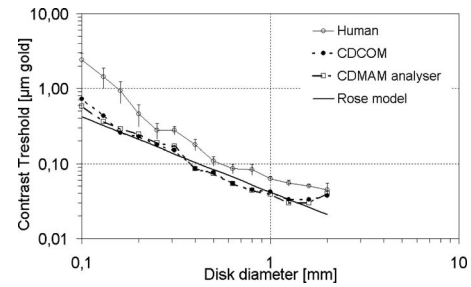


FIG. 12. Comparison of the CD curves for the RQA-M2 beam at an exposure of about $70 \mu\text{Gy}$. We plotted the curves obtained by three different techniques: Human observers, two automatic methods (CDCOM and CDMAM Analyser), and the theoretical Rose model [as described in Eq. (6)]. The error bars correspond to ± 1 standard error from the mean. The automatic readers give a remarkably better response than that from human observers in the entire range of diameters.

the lowest ones. In fact, the system quantum noise limit seems to be positioned at about 50–60 and 40–45 μGy for the RQA-M2 and the W/Rh beams, respectively. To our knowledge, these values are comparable to the quantum noise limit of other FPs. It is worth noting that the AMULET's NNPS values are up to two to three times lower than those from FFDM systems based on direct-conversion detectors and at the same time noticeably better than FPs based on scintillators. In particular, the improvement of the noise properties with respect to other FPs based on *a*-Se increases as the frequency increases.

The increased DQE outcomes of the W/Rh beam are mainly due to the better noise characteristics of this beam since the MTF is nearly identical to the RQA-M2 one. The fact that the use of tungsten beams can improve the image quality with respect to the traditional molybdenum beams agrees well with other studies.^{20,1} In particular, Hajdok *et al.* investigated the dependence of the Swank factor on x-ray energy and found out that a drop in the Swank factor (and, consequently, in the DQE) occurs at the *K* edge (i.e., about 12 keV for selenium).¹ This drop is due to backscatter escape of K-fluorescent photons and is responsible of an increase in the NNPS at this energy. Above this energy, this drop is recovered continuously, giving rise to an improvement of the DQE as the energy increases. This suggests that more energetic spectra (e.g., with W/Rh) might produce higher quality images than the traditional molybdenum beams. In fact, many digital systems are moving toward spectra with W/Rh anode/

TABLE II. Values of COR and IQF from the human reading and the automatic reading with CDCOM.

		Human readers	CDCOM
RQA-M2	COR (%)	58 ± 3	74
	IQF (mm μm)	22 ± 3	11
	$\text{IQF}_{\text{inv}} (\text{mm } \mu\text{m})^{-1}$	4.6 ± 0.7	8.8
W/Rh	COR (%)	63 ± 4	79
	IQF (mm μm)	19 ± 2	11
	$\text{IQF}_{\text{inv}} (\text{mm } \mu\text{m})^{-1}$	5.5 ± 0.6	8.8

filter combinations since this can improve the image quality or, alternatively, reduce the dose.^{21–23} To our knowledge, the DQE results obtained with AMULET are better than most of the published values for clinical FFDM systems.^{2–4,24} We believe that the very good behavior of the AMULET unit in terms of DQE is due to the combination of the good spatial resolution available for direct-conversion detectors, together with the excellent noise characteristics obtainable with the optical readout. The quantum noise limited condition can also be assessed by observing the exposure at which the DQE starts to decrease. These limits turn out to be around 50–60 μGy for RQA-M2 and 40–45 μGy for W/Rh and agree with those estimated from the product of NNPS with air kerma.

By estimating the DQE at the two orthogonal directions, it is possible to note that some differences arise, as a consequence of the variation in the MTF and NNPS, as already noted. These dissimilarities are marked especially at low frequencies, where a maximum difference of about 20% can be observed.

Despite its better DQE, no clear improvement emerges for the W/Rh beam and the difference between the CD curves obtained with the two beams is not statistically significant. However, in some cases W/Rh appears to provide a slightly better response than the RQA-M2 does, especially for large details. In fact, for details with a diameter greater than 0.7 mm the two curves are statistically different with $p < 0.02$. The comparison with some of the best published values demonstrates that the AMULET unit is able to provide a statistically significant better response for details with diameter greater than 0.35 mm ($p = 0.02$). For small details, results agree well with the best published.² The best CD results in that published paper were those achieved with a computed radiography unit (FUJIFILM FCR 5000 MA). That system was also the one with better noise properties. In fact, if we compare the AMULET CD results to its most similar system (*a*-Se FP), it turns out that the improvement is statistically significant ($p = 0.015$) for the entire range of details not only for large signals. We believe that the good noise characteristics of the AMULET system helps observers to improve the visibility of details since, as stated by Saunders *et al.*, “the quantum noise appears to be the dominant image quality factor in digital mammography, affecting radiologist performance.”²⁵ In fact, an increase in quantum noise can impede tasks such as the detection of microcalcifications and discrimination of benign and malignant masses.

The CD curve obtained with automatic methods agrees very well with the theoretical curve obtained by the Rose model. As also noted by other authors, this model matches with human data except for small details, where the effects of the human visual system become important and a more comprehensive model should be adopted for describing human observer results.^{2,13} The automatic reading results are comparable to those obtained on similar conditions for other FFDM systems.⁴

V. CONCLUSION

In this paper we presented physical and psychophysical characterizations of a novel FFDM clinical unit based on a direct-conversion detector with optical readout. The AMULET system showed MTF values of about 45% and 15% at 5 and 8 lp/mm, respectively. This result is slightly worse than other FFDM systems with *a*-Se plates but comparable to the MTF obtained with FPs based on scintillation phosphors. However, thanks to the optical reading, the novel system showed a NNPS decreasing with frequency which is two to three times lower than that obtained with FFDM systems based on *a*-Se detectors and noticeably better than FPs based on scintillators. The combination of good spatial resolution and excellent noise characteristics allows one to achieve better DQEs than those published for clinical FFDM systems. AMULET demonstrated DQEs of about 70% and 80% for the RQA-M2 and W/Rh beams, respectively. The investigated system presented a quantum noise limited condition comparable to other systems. In fact, these limits resulted to be about 50 μGy and 40 μGy for the RQA-M2 and W/Rh beams, respectively. The psychophysical analysis confirms the excellent behavior of the AMULET unit. Indeed, considering CD curves obtained by human observers, the investigated system gave better responses than those published for other FFDM systems. Also the COR and IQF values estimated for human readers and for automatic analysis with CDCOM software were better than those obtained on other FFDM systems tested under similar conditions.

ACKNOWLEDGMENTS

The authors would like to thank Satoshi Arakawa for his interest in the present work and for his helpful suggestions. The authors are also grateful to Dionigi Benincasa for the assistance in the revision of the manuscript.

^{a1}Author to whom correspondence should be addressed. Electronic mail: nico.lanconelli@unibo.it; URL: <http://www.bo.infn.it/~lanconelli/>; Telephone: +39-051-2095136; Fax: +39-051-2095047. Also at Dipartimento di Fisica, Viale Berti-Pichat 6/2, I-40127 Bologna (BO), Italy.

¹G. Hajdok, J. J. Battista, and I. A. Cunningham, “Fundamental x-ray interaction limits in diagnostic imaging detectors: Frequency-dependent Swank noise,” *Med. Phys.* **35**(7), 3194–3204 (2008).

²S. Rivetti, N. Lanconelli, R. Campanini, M. Bertolini, G. Borasi, A. Nitrosi, C. Danielli, L. Angelini, and S. Maggi, “Comparison of different commercial FFDM units by means of physical characterization and contrast-detail analysis,” *Med. Phys.* **33**(11), 4198–4209 (2006).

³B. Lazzari, G. Belli, C. Gori, and M. Rosselli Del Turco, “Physical characteristics of five clinical systems for digital mammography,” *Med. Phys.* **34**(7), 2730–2743 (2007).

⁴C. Ghetti, A. Borrini, O. Ortenzia, R. Rossi, and P. L. Ordonez, “Physical characteristics of GE Senographe Essential and DS digital mammography detectors,” *Med. Phys.* **35**(2), 456–463 (2008).

⁵J. A. Rowlands, D. M. Hunter, and N. Araj, “X-ray imaging using amorphous selenium: A photoinduced discharge readout method for digital mammography,” *Med. Phys.* **18**(3), 421–431 (1991).

⁶J. A. Rowlands and J. E. Taylor, “Design of a laser scanner for a digital mammography system,” *Med. Phys.* **23**(5), 755–758 (1996).

⁷N. Reznik, P. T. Komljenovic, S. Germann, and J. A. Rowlands, “Digital radiography using amorphous selenium: Photoconductively activated switch (PAS) readout system,” *Med. Phys.* **35**(3), 1039–1050 (2008).

⁸G. Pang, W. Zhao, and J. Rowlands, “Digital radiology using active matrix readout of amorphous selenium: Geometrical and effective fill factors,” *Med. Phys.* **25**(9), 1636–1646 (1998).

- ⁹International Electrotechnical Commission, "Medical diagnostic x-ray equipment—Radiation conditions for use in the determination of characteristics," IEC-61267, Geneva, Switzerland, 2003.
- ¹⁰K. Irisawa, K. Yamane, S. Imai, M. Ogawa, T. Shouji, T. Agano, Y. Hosoi, and T. Hayakawa, "Direct-conversion 50 μm pixel-pitch detector for digital mammography using amorphous selenium as a photoconductive switching layer for signal charge readout," *Proc. SPIE* **7258**, 7258111–72581110 (2009).
- ¹¹K. W. Jee, L. E. Antonuk, Y. El-Mohri, and Q. H. Zhao, "System performance of a prototype flat-panel imager operated under mammographic conditions," *Med. Phys.* **30**, 1874–1890 (2003).
- ¹²N. Karssemeijer and M. A. O. Thijssen, "Determination of contrast-detail curves of mammography systems by automated image analysis," *Proceedings of the IWDM 1996* (Elsevier, New York, 1996), pp. 155–160.
- ¹³N. W. Marshall, "A comparison between objective and subjective image quality measurements for a full-field digital mammography system," *Phys. Med. Biol.* **51**, 2441–2463 (2006).
- ¹⁴J. A. Rowlands, "The physics of computed radiography," *Phys. Med. Biol.* **47**, R123–R166 (2002).
- ¹⁵L. Riccardi, M. C. Cauzzo, R. Fabbris, E. Tonini, and R. Righetto, "Comparison between a built-in 'dual side' chest imaging device and a standard 'single side' CR," *Med. Phys.* **34**, 119–126 (2007).
- ¹⁶A. Mackenzie and I. D. Honey, "Characterization of noise sources for two generations of computed radiography systems using powder and crystalline photostimulable phosphors," *Med. Phys.* **34**(8), 3345–3357 (2007).
- ¹⁷International Electrotechnical Commission, "Medical electrical equipment—Characteristics of digital x-ray imaging devices—Part 1–2: Determination of the detective quantum efficiency—Detectors used in mammography," IEC-62220-1-2, Geneva, Switzerland, 2007.
- ¹⁸N. Lanconelli, S. Rivetti, P. Golinelli, M. Serafini, M. Bertolini, and G. Borasi, "Comparison of human observers and CDCOM software reading for CDMAM images," *Proc. SPIE* **6515**, 65150E1–65150E8 (2007).
- ¹⁹N. Lanconelli, S. Rivetti, P. Golinelli, R. Sansone, M. Bertolini, and G. Borasi, "Physical and psychophysical characterization of a GE Senographe DS clinical system," *Proc. SPIE* **6510**, 65104K1–65104K9 (2007).
- ²⁰R. S. Saunders, Jr., E. Samei, J. L. Jesneck, and J. Y. Lo, "Physical characterization of a prototype selenium-based full field digital mammography detector," *Med. Phys.* **32**(2), 588–599 (2005).
- ²¹P. Bernhardt, T. Mertelmeier, and M. Hoheisel, "X-ray spectrum optimization of full-field digital mammography: Simulation and phantom study," *Med. Phys.* **33**, 4337–4349 (2006).
- ²²J. M. Oduko, K. C. Young, O. Gundogdu, and A. Alsager, "Effect of using tungsten-anode x-ray tubes on dose and image quality in full-field digital mammography," *Lect. Notes Comput. Sci.* **5116**, 522–529 (2008).
- ²³P. Baldelli, N. Phelan, and G. Egan, "Effect of anode/filter combination on the dose and image quality of a digital mammography system based on an amorphous selenium detector," *Lect. Notes Comput. Sci.* **5116**, 716–723 (2008).
- ²⁴P. Monnin, D. Gutierrez, S. Bulling, D. Guntern, and F. R. Verdun, "A comparison of the performance of digital mammography systems," *Med. Phys.* **34**(3), 906–914 (2007).
- ²⁵R. S. Saunders, Jr., J. A. Baker, D. M. Delong, J. P. Johnson, and E. Samei, "Does image quality matter? Impact of resolution and noise on mammographic task performance," *Med. Phys.* **34**, 3971–3981 (2007).